ACS OMEGA

http://pubs.acs.org/journal/acsodf

Article

Hydrogen Generation over RuO_2 Nanoparticle-Decorated $LaNaTaO_3$ Perovskite Photocatalysts under UV Exposure

Maha Alhaddad, Adel A. Ismail,* and Zaki I. Zaki

Cite This: *ACS Omega* 2021, 6, 10250−10259

Read Online

ACCESS | Metrics & More | Article Recommendations

ABSTRACT: The efficacy of $LaNaTaO_3$ perovskites decoration RuO_2 at diverse contents for the photocatalytic H_2 generation has been explored in this study. The photocatalytic performance of RuO_2 co-catalyst onto mesoporous $LaNaTaO_3$ was evaluated for H_2 under UV illumination. 3%RuO_2/$LaNaTaO_3$ perovskite photocatalyst revealed the highest photocatalytic H_2 generation performance, indicating that RuO_2 nanoparticles could promote the photocatalytic efficiency of $LaNaTaO_3$ perovskite significantly. The H_2 evolution rate of 3%RuO_2/$LaNaTaO_3$ perovskite is 11.6 and 1.3 times greater than that of bare $LaNaTaO_3$ perovskite employing either 10% CH_3OH or pure H_2O, respectively. Interestingly, the photonic efficiency of 3%RuO_2/$LaNaTaO_3$ perovskite was enhanced 10 times than $LaNaTaO_3$ perovskite in the presence of aqueous CH_3OH solutions as a hole sacrificial agent. The high separation of charge carriers is interpreted by the efficient hole capture using CH_3OH, hence leading to greater H_2 generation over RuO_2/$LaNaTaO_3$ perovskites. This is attributed to an adjustment position between recombination electron−hole pairs and also the reduction of potential conduction alignment as a result of RuO_2 incorporation. The suggested mechanisms of RuO_2/$LaNaTaO_3$ perovskites for H_2 generation employing either CH_3OH or pure H_2O were discussed. The photocatalytic performances of the perovskite photocatalyst were elucidated according to the PL intensity and the photocurrent response investigations.

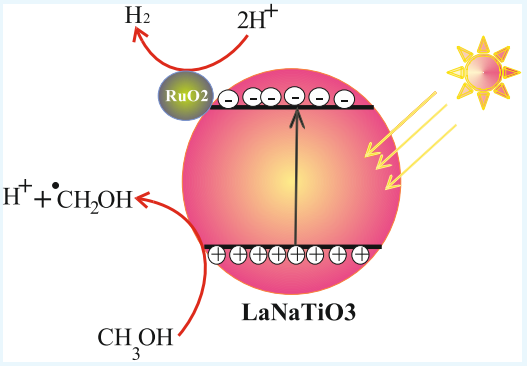

INTRODUCTION

With the growth of the industrial and scientific community, the photocatalyst as a favorable semiconductor material is considered as a promising and hot theme of research studies owing to its wide implementations in considerable fields, particularly for energy saving and environmental protection.[1−3] Photocatalytic production of molecular hydrogen through semiconductor materials as efficient photocatalysts is considered as a promising avenue to produce sustainable and clean energy,[1−3] and promoting semiconductor materials under visible light with a high photonic efficiency for the conversion of solar energy to molecular hydrogen is ultimately desired for potential applications.[4−6] Recently, water splitting to generate molecular hydrogen employing perovskite oxide materials (ABO_3) has attracted increasing attention with a high photonic efficiency. Among ABO_3 perovskite oxide materials, the $NaTaO_3$ photocatalyst has been realized for hydrogen generation from H_2O using UV irradiation.[7−16] The band gap of $NaTaO_3$ is 4.0 eV, and it can be synthesized by diverse approaches, for instance, solid-state,[7−9,13,16] molten salt,[17] sol−gel,[11] and hydrothermal methods.[10,13−15]

To promote the photocatalytic activity of $NaTaO_3$ particles, numerous scientists have made great effort to employ other synthetic avenues to obtain $NaTaO_3$ nanoparticles as efficient photocatalysts. $NaTaO_3$ as a colloidal array was synthesized using carbon mesopores as a direct structure agent for casting that was reproduced using silica nanosphere configuration.[14] The mesoporous carbon matrix was eliminated by calcination, and then $NaTaO_3$ nanoparticles as a colloidal array were obtained with a 34 m^2 g^{-1} surface area and a 20 nm particle size. The obtained $NaTaO_3$ prepared by this approach exhibited a 3 times higher photocatalytic efficiency than that prepared from the traditional hydrothermal synthesis for overall water splitting.[14] $NaTaO_3$ nanoparticles with ∼25 nm crystallite size, synthesized by an exo-template method, exhibited an ∼20 times higher hydrogen production rate than those synthesized using the solid-state approach.[16]

The recombination of photogenerated holes and electrons of large $NaTaO_3$ nanoparticles was faster than those in smaller $NaTaO_3$ nanoparticles with high crystallinity. On the other hand, much effort was made to perform a greater photonic efficiency of lanthanide-doped $NaTaO_3$.[18−22] The pho-

Received: February 1, 2021
Accepted: March 31, 2021
Published: April 8, 2021

tonic efficiency of $NaTaO_3$ is greatly promoted by employing a co-catalyst such as Ru, NiO, Pt, or Rh, loaded on the $NaTaO_3$ surface.[23−28] In general, loading of co-catalysts at different contents onto the photocatalyst surface led to a significant boost of molecular H_2 production compared with pure photocatalysts. A co-catalyst serves as a trapping agent of electrons, which produces a prolonged lifetime of photo-induced charge carriers, reducing their recombination rate. In terms of the co-catalyst-loaded semiconductor photocatalyst preparation, it is concluded that the crystalline structure of the prepared photocatalysts is very susceptible to synthetic approaches such as solid-state,[11,29,30] solvothermal,[30] sol−gel,[30] hydrothermal,[12,31,32] alkalide reduction,[33] flux,[34] and electrospinning methods.[35] $NaTaO_3$-based photocatalysts were synthesized via the traditional solid-state and sol−gel approaches. The conventional solid-state approach needs elevated annealing temperatures to produce $NaTaO_3$ with orthorhombic structure, whereas the sol−gel avenue requires low temperatures during the preparation to obtain $NaTaO_3$ with a monoclinic structure.[10,36,37] Also, $NaTaO_3$-based photocatalysts could be prepared by the hydrothermal process.[37,38] Efficient separation and inhibition recombination of charge carriers are paramount for H_2O splitting to create molecular H_2. In addition, separation and fabrication of active sites for H_2 generation are indispensable. Obviously, incorporation of RuO_2 co-catalysts onto $NaTaO_3$ perovskite surface is substantial for boosting their photonic efficiency for the production of molecular hydrogen. The photonic efficiency of $NaTaO_3$-based photocatalysts could be considerably calculated by doping foreign ions in the $NaTaO_3$ lattice.

Therefore, in the present proposal, synthesis of mesoporous RuO_2/$LaNaTaO_3$ perovskites at different RuO_2 contents for molecular H_2 generation was investigated employing the CH_3OH/H_2O system. The H_2 evolution rate of 3%RuO_2/$LaNaTaO_3$ perovskite is 11.6 and 1.3 times greater than that of the $LaNaTaO_3$ perovskite employing 10% methanol pure H_2O, respectively. Interestingly, the photonic efficiency of 3%RuO_2/$LaNaTaO_3$ perovskite was enhanced 10 times compared to $LaNaTaO_3$ perovskite in the presence of aqueous CH_3OH solutions. The suggested mechanisms of RuO_2/$LaNaTaO_3$ perovskites for H_2 evolution employing aqueous CH_3OH solutions and pure H_2O were discussed. The photocatalytic performances of perovskite photocatalyst were evaluated according to the PL intensity and the photocurrent response investigations.

RESULTS AND DISCUSSION

Perovskite Investigations. X-ray diffraction patterns of $LaNaTaO_3$and RuO_2/$LaNaTaO_3$ perovskites at different RuO_2 contents were investigated, as shown in Figure 1. The XRD pattern of $LaNaTaO_3$ perovskite was assigned as the monoclinic structure of the synthesized $LaNaTaO_3$ perovskite. The peaks at 22.91, 32.36, 40.04, 46.71, 52.61, 58.17, 68.08, 72.9, and 77.4° (Figure 1a) have corresponded to the planes of (100), (101), (111), (200), (102), and (121) (JCPDS no. 74-2478). After addition of RuO_2 at different contents of 0.5, 1, 3, and 5%, the intensity of the mean peak is gradually decreased with increasing RuO_2 content (Figure 1b−d). It is documented that the ionic radii of La^{3+} (1.36 Å) and Na^{+} (1.39 Å) ions are equivalent.[39] In addition, the ionic radius of the Ta^{5+} ion (0.64 Å) is notably smaller than that of the La^{3+} ion (1.032 Å).[39] If Ta^{5+} ions were replaced with La^{3+} ions at the B site position in the perovskite structure, a considerable shift should be

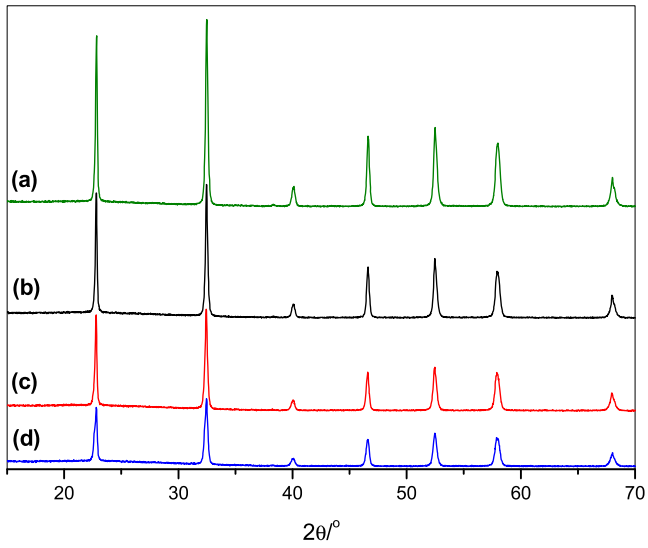

Figure 1. X-ray diffraction peaks around 32.5° of (a) $LaNaTaO_3$ and $LaNaTaO_3$ doped with RuO_2: (b) 1%, (c) 3%, and (d) 5%.

recognized. Interestingly, there was no crystalline phase involving RuO_2 at different RuO_2 concentrations of 0.5−5% that could be detected, indicating that RuO_2 nanoparticles are highly contributed over the mesoporous $La_{0.02}Na_{0.98}TaO_3$ network with a small particle size. This is attributed to the adsorption of the Ru(III)−acetylacetonate complex onto the $La_{0.02}Na_{0.98}TaO_3$ surface, and then the obtained powder was annealed at 450 °C and the adsorbed Ru(III)−acetylacetonate complex was decomposed to RuO_2 nanoparticles onto the surface of the $LaNaTaO_3$ perovskite network and inside the walls of the pores. The possibility of interaction (substitution of Ru^{4+} for Ta^{5+}) between equivalent ionic radii materials Ru^{4+} (0.62 Å) and Ta^{5+} (0.64 Å) could partly explain this observation.

Figure 2 shows SEM images of (a) bare $LaNaTaO_3$ perovskite and RuO_2/$LaNaTaO_3$ at 0.5% (b), 1% (c), 3% (d), and 5% (e) loadings. The ordered surface nanostructure of the $LaNaTaO_3$ perovskite was self-constructed as shown in Figure 2a. The particle sizes of the $LaNaTaO_3$ perovskite were enlarged on increasing the RuO_2 content from 0.5 to 5% (Figure 2b−e). These characteristics are advantageous in terms of small particle size and high crystallinity for the enhanced photocatalytic efficiency of perovskite photocatalysts. EDS analysis showed the presence of Ru, La, Na, and O and proved that the RuO_2/$LaNaTaO_3$ perovskite consisted of the precursor ratios employed in the starting mixtures. The EDS quantitative analysis of 1%RuO_2/$LaNaTaO_3$ shows that the weight percents of Ru, La, Na, Ta, and O are 0.08, 0.42, 16.91, 18.90, and 63.68, respectively. Figure 3 displays the TEM images of the structure and morphology of mesoporous $LaNaTaO_3$, and 3%RuO_2/$LaNaTaO_3$ perovskite. The $LaNaTaO_3$ perovskite particles were highly dispersed with uniform shape and size (∼10 nm) as clearly displayed in Figure 3a. The morphology of the 3%RuO_2/$LaNaTaO_3$ NPs is similar to the bare $LaNaTaO_3$ perovskite in terms of shape and size (Figure 3b). The atomic planes of RuO_2 and $NaTaO_3$ NPs were estimated at 3.2 and 3.80 Å, respectively, which matches to the lattice spacing of (110) and (111), as obviously depicted in Figure 3c, and the $NaTaO_3$ and RuO_2 NPs are connected, along with the well matching of selected area electron diffraction of $NaTaO_3$ perovskite with the orthorhombic

https://doi.org/10.1021/acsomega.1c00584
ACS Omega 2021, 6, 10250−10259

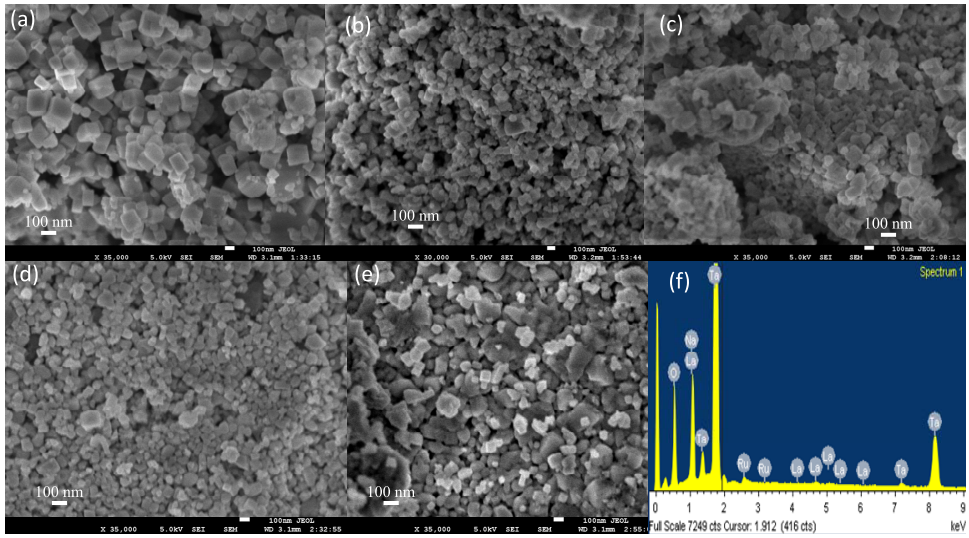

Figure 2. Scanning electron microscope images of (a) $LaNaTaO_3$ and $LaNaTaO_3$ doped with RuO_2: (b) 0.5%, (c) 1%, (d) 3%, and (e) 5%. (f) EDS pattern of 1%RuO_2-doped La/$NaTaO_3$.

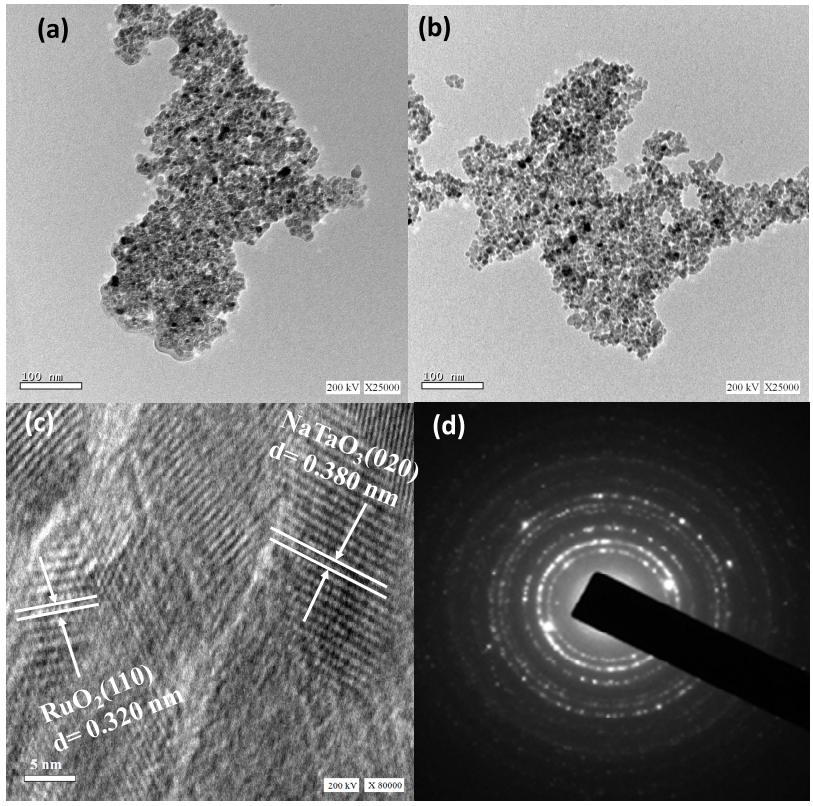

Figure 3. TEM images of bare $LaNaTaO_3$ (a) and 3%RuO_2/$LaNaTaO_3$ nanocomposite (b). HRTEM image of mesoporous 3%RuO_2/$LaNaTaO_3$ nanocomposite (c). Selected area electron diffraction of 3%RuO_2/$LaNaTaO_3$ (d).

crystal (Figure 3d). The high crystallinity of the synthesized RuO_2/$LaNaTaO_3$ perovskite was confirmed by clear lattice spacing of atomic planes (Figure 3d).

Nitrogen adsorption isotherms of the bare $LaNaTaO_3$ and 3%RuO_2/$LaNaTaO_3$ perovskites are depicted in Figure 4. The adsorption isotherms of both $LaNaTaO_3$ and 3%RuO_2/$LaNaTaO_3$ perovskites are of typical reversible type IV. The inflection sharpness was obtained at relative pressures in the capillary condensation range of 0.45−0.7, resulting in mesostructured materials. The mesopores were formed as a result of interparticle voids between prepared nanoparticles. The mesoporosity can be explained by the formation of irregular voids between $LaNaTaO_3$ particles. In addition, the existence of voids among $LaNaTaO_3$ NPs participates in boosting the surface area of the prepared $LaNaTaO_3$ photocatalyst. The BET surface area of 3%RuO_2/$LaNaTaO_3$ perovskite was calculated to be 34 $m^2\ g^{-1}$.

XPS spectroscopy was used to examine the states and composition of the 1%RuO_2/$LaNaTaO_3$ photocatalyst as displayed in Figure 5. Figure 5a shows two peaks located at

https://doi.org/10.1021/acsomega.1c00584
ACS Omega 2021, 6, 10250−10259

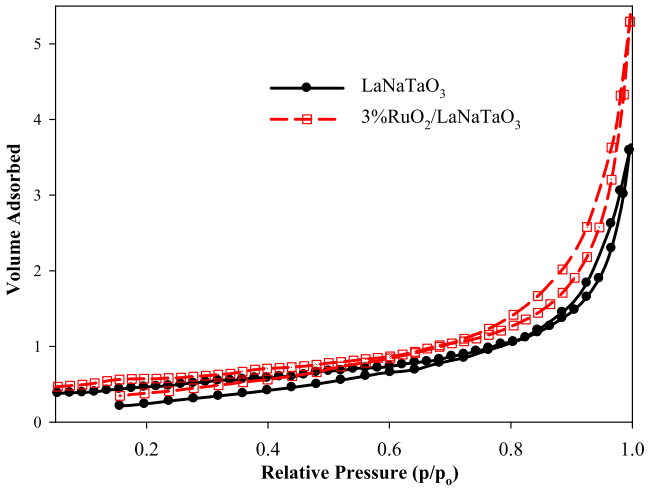

Figure 4. N_2 sorption isotherms of the mesoporous $LaNaTaO_3$ and $1\%RuO_2/LaNaTaO_3$.

838.45 and 834.45 eV for La $3d_{3/2}$ and La $3d_{5/2}$, respectively, which are comparable to the existence of La^{3+} in $LaNaTaO_3$. As displayed in Figure 4b, the Ru 3d spectrum exhibited two mean peaks centered at 284.44 and 279.62 eV referred to Ru $3d_{3/2}$ and Ru $3d_{5/2}$, respectively, emphasizing the presence of Ru in the Ru^{4+} form. Figure 5c shows two peaks at 1 and 27.9 eV for the Ta 4f spectrum, confirming the existence of Ta in the Ta^{5+} form.[40] It is attributed to one mean peak for the O 1s spectrum at 530.1 eV, which is confirmed to the presence of O atoms in the $LaNaTaO_3$ crystal lattice; besides, there are other two peaks centered at 531.4 and 532.5 eV, leading to the presence of ^{-}OH surface and adsorbed O (Figure 5d), respectively.[41] The Na 1s peak is located at ~1071.3 eV, identifying the Na^+ oxidation state, as obviously seen in Figure 5e. The XPS results confirmed that the prepared perovskite was composed of Ru^{4+}, Na^+, La^{3+}, Ta^{5+}, and oxygen in the crystal lattice, and their atomic percentages were determined to be approximately 0.98, 7.87, 1.98, 70.82, and 19.05%, respectively.

The UV−vis spectra of bare $LaNaTaO_3$ and $RuO_2/LaNaTaO_3$ perovskites were examined to demonstrate the effects of Ru^{4+} doping on the band gap structure modulation of the $LaNaTaO_3$ perovskites shown in Figure 6. The DRS of the prepared photocatalysts displayed a broad absorption in the UV region (250−320 nm), leading to the electronic transformation from O 2p to the Ta 5d orbitals. The absorption spectrum of Ru^{4+}-doped $LaNaTaO_3$ perovskite is different from that of $LaNaTaO_3$ perovskite (Figure 6a). The Ru^{4+}-doped $LaNaTaO_3$ perovskite sample revealed a superficial peak in the range of 450−600 nm with higher intensities (Figure 6a). The direct optical band gap energy of $RuO_2/LaNaTaO_3$ photocatalysts at different RuO_2 contents can be calculated as follows: $\alpha h\nu = A(h\nu - E_g)^{1/2}$, where α, E_g, $h\nu$, A, and n are the absorption coefficient, band gap energy, photon energy, constant, and incident light, respectively.[24] Band gap energy was estimated to be ~4.08−4.01 eV corresponding to the absorption in the 307−310 nm region with the increase of RuO_2 content as depicted in Figure 6b. The calculated band gap energies of the RuO_2 loading $LaNaTaO_3$ perovskite photocatalysts with various RuO_2 contents are listed in Table 1. The addition of RuO_2 did not change the absorption band for $LaNaTaO_3$; thus, the band gap values are very close.

Photocatalytic Performance. Photocatalytic tests were conducted on mesoporous $RuO_2/LaNaTaO_3$ perovskites for H_2 generation from either CH_3OH or pure H_2O. The RuO_2 loading $LaNaTaO_3$ perovskite at different contents (0−5%) was assessed for H_2 generation from either pure H_2O or CH_3OH (10 vol %). The illumination time of the photocatalytic H_2 evolution was conducted over the obtained photocatalysts employing pure H_2O and CH_3OH, as illustrated in Figure 7a,b. The findings exhibited that the H_2 evolution immediately started as the UV lamp was turned on. H_2 evolution rates were reached to steady state within 30 min. At this stage, the photocatalytic reaction was illuminated for 6 h to detect and determine the H_2 evolution rate. Finally, the UV lamp was turned off, and the H_2 evolution abruptly declined to reach the baseline (Figure 7a,b). The H_2 evolution rates were calculated by subtracting the baseline and average of the values obtained from the curve with almost steady rates of H_2 evolution, as shown in Figure 7. The findings indicated that there was no H_2 evolution without using the photocatalysts. It can be seen that the mesoporous $LaNaTaO_3$ perovskite photocatalyst exhibits the minimum photocatalytic performance. The H_2 evolution ultimately increased when RuO_2 was grafted onto $LaNaTaO_3$ perovskite surface. In addition, the photocatalytic efficiency of the $LaNaTaO_3$ perovskite was enhanced with the increment of the RuO_2 content, achieving the highest H_2 evolution at 3% RuO_2.

Figure 8a exhibits H_2 evolution rates evolution over $LaNaTaO_3$ perovskite loading different RuO_2 contents (0, 0.5, 1, 3, and 5%), from pure H_2O and from 10% CH_3OH. The H_2 evolution rate was increased from 0 to 1.29 μmol h^{-1} when pure H_2O was used with the increase of RuO_2 content from 0 to 5%. However, in the case of 10% methanol, the H_2 evolution rate was improved from 0.99 to 11.54 μmol h^{-1} with the increase of RuO_2 content from 0 to 5%. Interestingly, the H_2 evolution rate of $3\%RuO_2/LaNaTaO_3$ perovskite is the fastest among all of the synthesized photocatalysts. Besides, the H_2 evolution rate of $3\%RuO_2/LaNaTaO_3$ perovskite is 11.6 times greater than that of $LaNaTaO_3$ employing 10% methanol; however, in the case of pure H_2O, the H_2 evolution rate of 3% $RuO_2/LaNaTaO_3$ perovskite was enhanced 1.3 times than $LaNaTaO_3$. Also, the H_2 evolution rate of $3\%RuO_2/LaNaTaO_3$ employing 10% methanol is 9 times higher than employing pure H_2O. Figure 8b shows the photonic efficiency of $RuO_2/LaNaTaO_3$ perovskite at different RuO_2 contents (0.5, 1, 3, and 5%), from pure water and 10% methanol. The results revealed that the photonic efficiency was increased from 0 to 1.5 with the increase of the RuO_2 content from 0 to 5% employing pure water; however, the photonic efficiency was increased from 0.2 to 2% with increasing the RuO_2 content from 0 to 3%; then, it was decreased to 1.7% at $5\%RuO_2$ using 10% methanol. Interestingly, the photonic efficiency of 3% $RuO_2/LaNaTaO_3$ perovskite was enhanced 10 times than bare $LaNaTaO_3$ perovskite. Table 2 summarizes the comparison between the synthesized photocatalysts and other samples for photocatalytic H_2 generation.

It is supposed that the high RuO_2 content can cover $LaNaTaO_3$ perovskite surface, suggesting reduction of the photoexciting capability of the $LaNaTaO_3$ perovskite photocatalyst.[42] In addition, it could be caused by the agglomeration and growth of RuO_2 onto mesoporous $LaNaTaO_3$ perovskite surface and hence weakened the role of the co-catalyst.[24,43] The $3\%RuO_2/LaNaTaO_3$ perovskite revealed the maximum photocatalytic performance among all of the synthesized

https://doi.org/10.1021/acsomega.1c00584
ACS Omega 2021, 6, 10250−10259

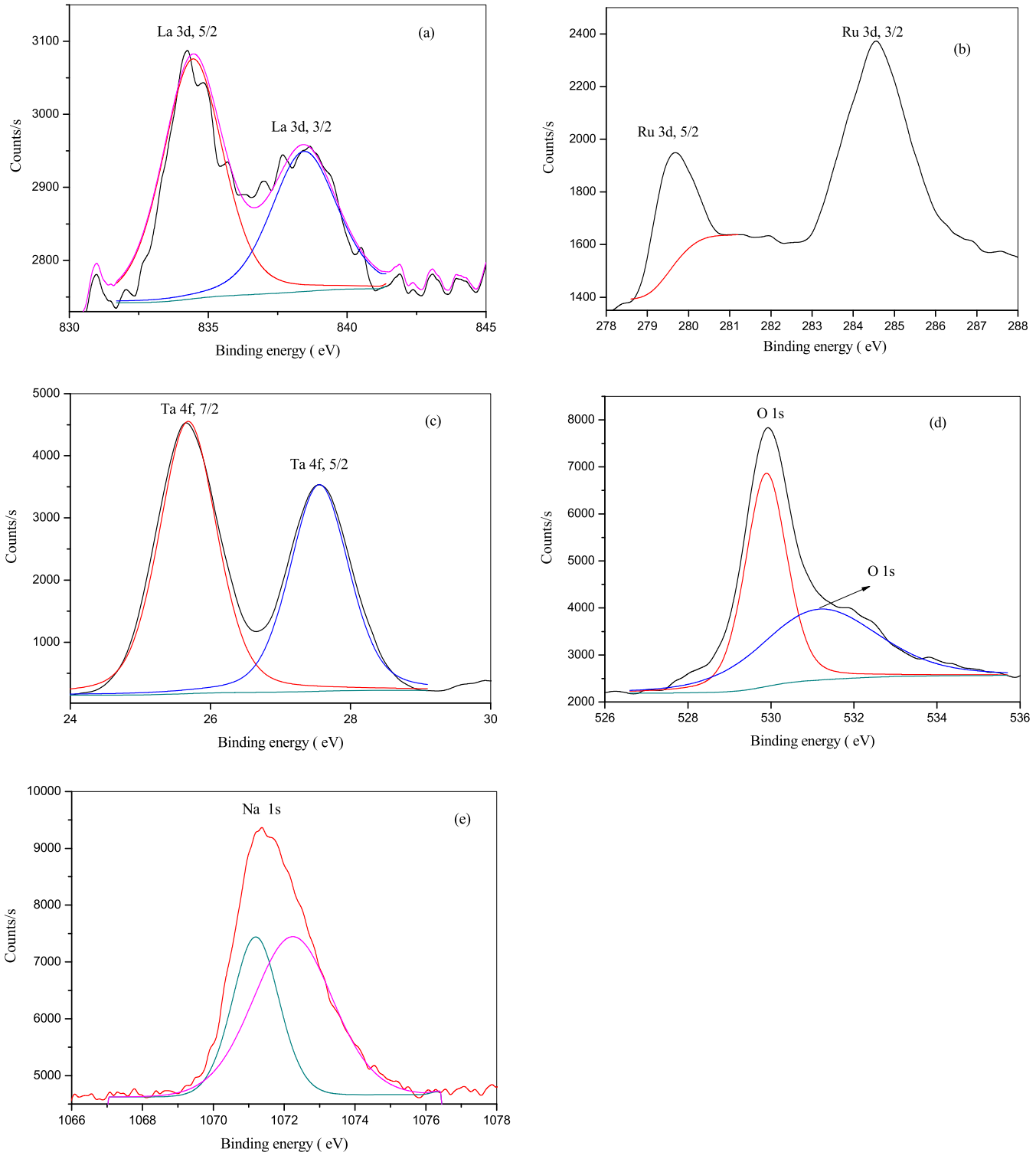

Figure 5. XPS analysis of 1%RuO_2/$LaNaTaO_3$ exhibiting the high-resolution spectra for La 3d (a), Ru 3d (b), Ta 4f (c), O 1s (d), and Na 1s (e).

photocatalysts, indicating that the incorporation of RuO_2 could promote the photocatalytic activity of $LaNaTaO_3$ perovskite significantly. The improved photocatalytic performance of the RuO_2/$LaNaTaO_3$ perovskite photocatalyst was explained by the effective separation of charge carriers in the present RuO_2/$LaNaTaO_3$ perovskite that is accomplished by exciting the electrons from the VB to the CB of $LaNaTaO_3$. Then, the photogenerated electrons migrate to RuO_2 NPs (Scheme 1). The addition of RuO_2 nanoparticles onto the $LaNaTaO_3$ perovskite leads to prepared materials possessing Brønsted acids with the distinguishing interaction of the Ru−O···H bond, However, the acid strength onto the surface of RuO_2 attributes to its capability to eliminate a proton. It is documented that RuO_2 possesses the highest electronegativity, small particle size, and the highest oxidation state (IV).[44] Therefore, RuO_2 has the strongest Brønsted acid and shows the maximum photocatalytic performances for H_2 evolution in both CH_3OH solution and pure H_2O due to the prohibition of

https://doi.org/10.1021/acsomega.1c00584
ACS Omega 2021, 6, 10250−10259

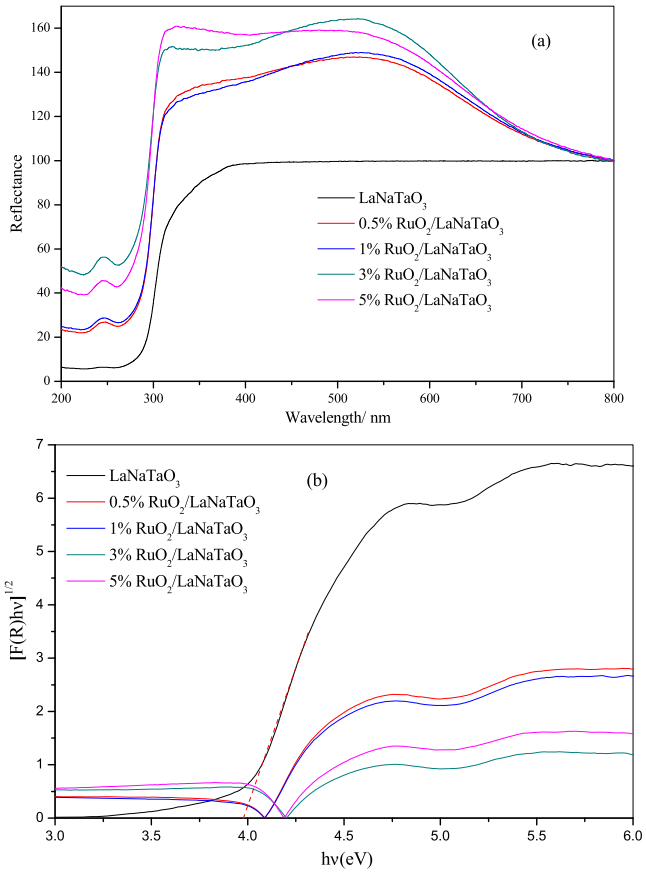

Figure 6. (a) Diffuse reflectance spectra of $LaNaTaO_3$ and $LaNaTaO_3$ doped with RuO_2 at varying contents. (b) Plot of transferred Kubelka–Munk versus energy of $LaNaTaO_3$ and $LaNaTaO_3$ doped with RuO_2 at varying contents.

Table 1. Hydrogen Production from Methanol and Water over Mesoporous $RuO_2/LaNaTaO_3$ Photocatalyst at Different RuO_2 Contents

photocatalysts	band gap (eV)	H_2 evaluation rate (μmol h^{-1})		PE (%)	
		H_2O	CH_3OH	H_2O	CH_3OH
$LaNaTaO_3$	3.98 ± 01	0.00	0.99	0.00	0.02
0.5%RuO_2/ $LaNaTaO_3$	4.08 ± 01	0.88	10.96	0.02	0.19
1%$RuO_2/LaNaTaO_3$	4.08 ± 01	1.07	9.66	0.02	0.16
3%$RuO_2/LaNaTaO_3$	4.18 ± 01	1.26	11.54	0.02	0.20
5%$RuO_2/LaNaTaO_3$	4.18 ± 01	1.29	8.81	0.17	0.15

the unwanted backreaction of O_2 with H_2 resulting in H_2O onto the RuO_2 surface.[44,45]

To confirm the reason for the promotion of the photocatalytic activity of $RuO_2/LaNaTaO_3$ perovskites, photocurrent response and photoluminescence (PL) were measured. The photocurrent response over $LaNaTaO_3$ and $RuO_2/LaNaTaO_3$ perovskites is depicted in Figure 9a in the dark and under illumination. In the dark, there was no response current; however, upon illumination, bare $LaNaTaO_3$ perovskite revealed the lowest photoresponse. With the increase of RuO_2 from 1 to 3%, the photocurrent intensity was increased gradually decreased at 5%$RuO_2/LaNaTaO_3$ perovskite, implying the high tendency upon illumination to facilitate the separation of photo-created electrons and holes. This result is

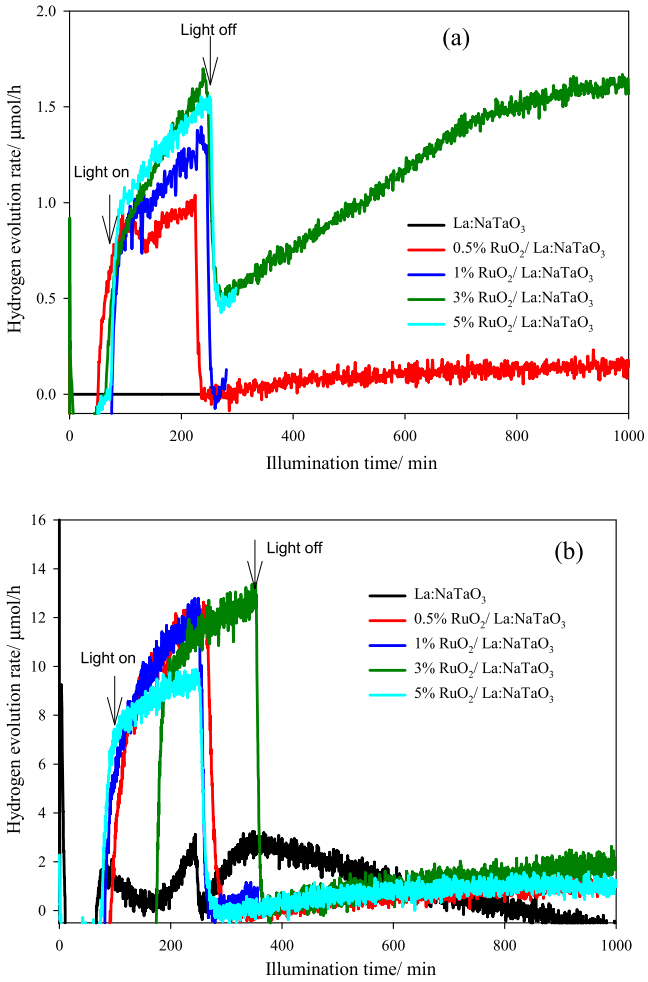

Figure 7. Time course of photocatalytic H_2 evolution over $LaNaTaO_3$ perovskite loading different RuO_2 contents (0.5, 1, 3, and 5%), from pure water (a) and 10% methanol (b).

consistent and explained the photocatalytic H_2 generation. The PL of bare $LaNaTaO_3$ and $RuO_2/LaNaTaO_3$ perovskites at diverse RuO_2 percentages is displayed in Figure 9b. The PL peak of bare $LaNaTaO_3$ perovskite was assigned at $\lambda \sim 469.34$ nm with a higher PL intensity. However, the PL intensity of the $RuO_2/LaNaTaO_3$ perovskites revealed a lower intensity than bare $LaNaTaO_3$ perovskite. The $RuO_2/LaNaTaO_3$ perovskites exhibited a low exciton emission owing to the expedition of charge carrier separation. Interestingly, the PL intensity of $RuO_2/LaNaTaO_3$ perovskites decreased with the increase of RuO_2 content, presenting photoinduced electron transfer from the CB of $LaNaTaO_3$ perovskites to the close contact RuO_2 NPs.

The mechanism of highly effective H_2 evolution over $RuO_2/LaNaTaO_3$ photocatalysts in pure H_2O and CH_3OH was demonstrated in Scheme 1. After UV illumination, the generated electrons and holes move in a prolonged space to reach the active sites of the RuO_2 surface. As the RuO_2 nanoparticle is decreased in terms of size, the probability of the surface reaction of the generated electrons and holes with adsorbed methanol and water molecules is boosted compared to that of the bulk recombination of charge carriers.[27] At the conduction band of $LaNaTaO_3$ perovskite, the adsorbed H_2O molecules can be effectively reduced to molecular H_2 onto RuO_2 nanoparticles. The ordered surface $RuO_2/LaNaTaO_3$

https://doi.org/10.1021/acsomega.1c00584
ACS Omega 2021, 6, 10250−10259

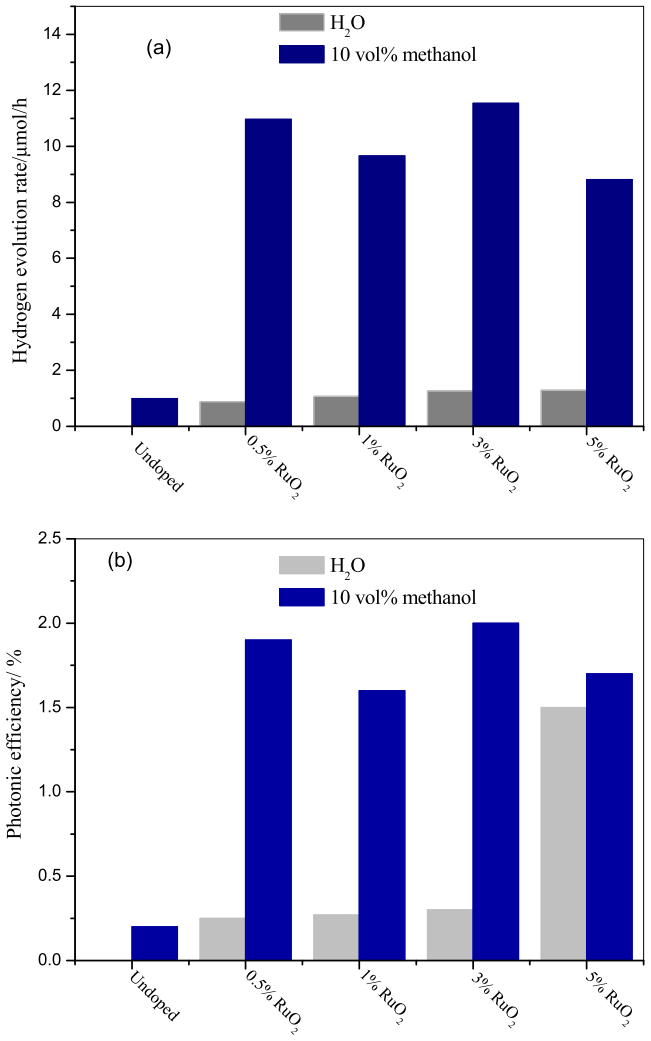

Figure 8. (a) H_2 evolution rates evolution over $LaNaTaO_3$ loading different RuO_2 contents (0.5, 1, 3, and 5%) from pure water and from 10% methanol. (b) Photonic efficiency of $LaNaTaO_3$ and RuO_2 loading $LaNaTaO_3$ at different contents (0.5, 1, 3, and 5%) from pure water and from 10% methanol.

perovskite with a small particle size has promoted the suppression of carrier recombination and of active site separation to prohibit the backward reaction of O_2 with H_2, indicating the highly effective H_2O splitting. In the case of CH_3OH as a sacrificial agent, the mechanism is not clear because it is not determined whether the movement of electrons from the reduction of $^{\bullet}CH_2OH$ radical or conduction band of $LaNaTaO_3$ perovskite is the rate-limiting step or if the photocatalytic activity might be determined by transporting hole to the CH_3OH.[44,46]

Scheme 1. Schematic Demonstration of Hydrogen Production over Mesoporous $RuO_2/La_{0.02}Na_{0.98}TaO_3$ Photocatalyst in the Presence of Methanol

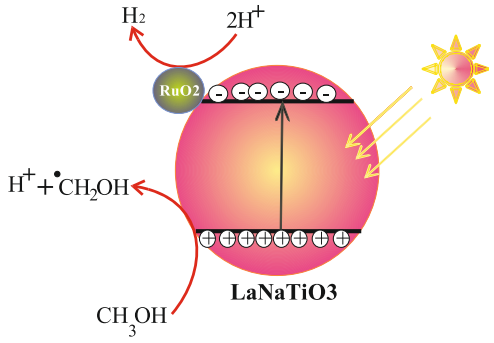

CONCLUSIONS

Synthesis of mesoporous $RuO_2/LaNaTaO_3$ perovskites at different RuO_2 contents for the generation of molecular H_2 was investigated employing the CH_3OH/H_2O system. The XRD findings show that mesoporous $LaNaTaO_3$ perovskite was formed as the monoclinic structure. The adsorption isotherms of $LaNaTaO_3$ perovskite type IV result in a mesopores structure. The H_2 evolution rate in the case of pure H_2O was increased from 0 to 1.29 μmol h^{-1} with the increase of RuO_2 content from 0 to 5%. However, in the case of 10% methanol, the H_2 evolution rate was increased from 0.99 to 11.54 μmol h^{-1} with the increase of the RuO_2 content from 0 to 5%. The H_2 evolution rate of $3\%RuO_2/LaNaTaO_3$ is the fastest among all of the synthesized photocatalysts. The H_2 evolution rate of the $3\%RuO_2/LaNaTaO_3$ perovskite is 11.6 times higher than that of $LaNaTaO_3$ employing 10% methanol; however, in the case of pure H_2O, the H_2 evolution rate of the $3\%RuO_2/LaNaTaO_3$ perovskite was enhanced 1.3 times than $LaNaTaO_3$. The H_2 evolution rate of the $3\%RuO_2/LaNaTaO_3$ perovskite employing 10% methanol is 9 times higher than employing pure H_2O. The photonic efficiency of the $3\%RuO_2/LaNaTaO_3$ perovskite was enhanced 10 times than $LaNaTaO_3$.

EXPERIMENTAL SECTION

Materials. Ruthenium(III) acetylacetonate, $Ru(acac)_3$, sodium acetate CH_3COONa, CH_3COOH, $Ti(OC(CH_3)_3)_4$ (TBOT), lanthanum nitrate, $La(NO_3)_3{\cdot}xH_2O$, tantalum(V) chloride, $TaCl_5$, HCl, CH_3OH, F-127 pluronic (EO_{106}-$PO_{70}EO_{106}$, MW 12 600 g mol^{-1}), and C_2H_5OH were procured from Sigma-Aldrich.

Preparation of Mesoporous $RuO_2/LaNaTaO_3$ Perovskites. Mesoporous $La_xNa_{1-x}TaO_3$ (x = 0.02) perovskites were synthesized via a wet chemical approach employing F127 copolymer as a proper template. La and Na nanoparticles were homogeneously distributed into the tantalum oxide framework

Table 2. Comparison between Photocatalytic H_2 Generation over the Synthesized Photocatalyst in the Present Work and Other $LaNaTaO_3$ Photocatalysts

photocatalysts	reaction medium	light source	generation H_2 rate	references
$NiO/La_xNa_{1-x}TaO_3$	CH_3OH	UV	26.94 mmol g^{-1} h	23
$2\%Ag/La_{0.02}Na_{0.98}TaO_3$	glycerol	UV	332.43 μmol g^{-1} h^{-1}	24
$1\%Pt/La_{0.02}Na_{0.98}TaO_3$	glycerol	UV	86.16 μmol g^{-1} h^{-1}	25
$0.6\%Nd_2O_3/LaNaTaO_3$	glycerol	UV	95 μmol g^{-1} h^{-1}	26
$1\%In_2O_3/La_{0.02}Na_{0.98}TaO_3$	glycerol	UV	235 μmol g^{-1} h^{-1}	27
$3\%RuO_4/La_{0.02}Na_{0.98}TaO_3$	CH_3OH	UV	11.54 μmol h^{-1}	this work

https://doi.org/10.1021/acsomega.1c00584
ACS Omega 2021, 6, 10250−10259

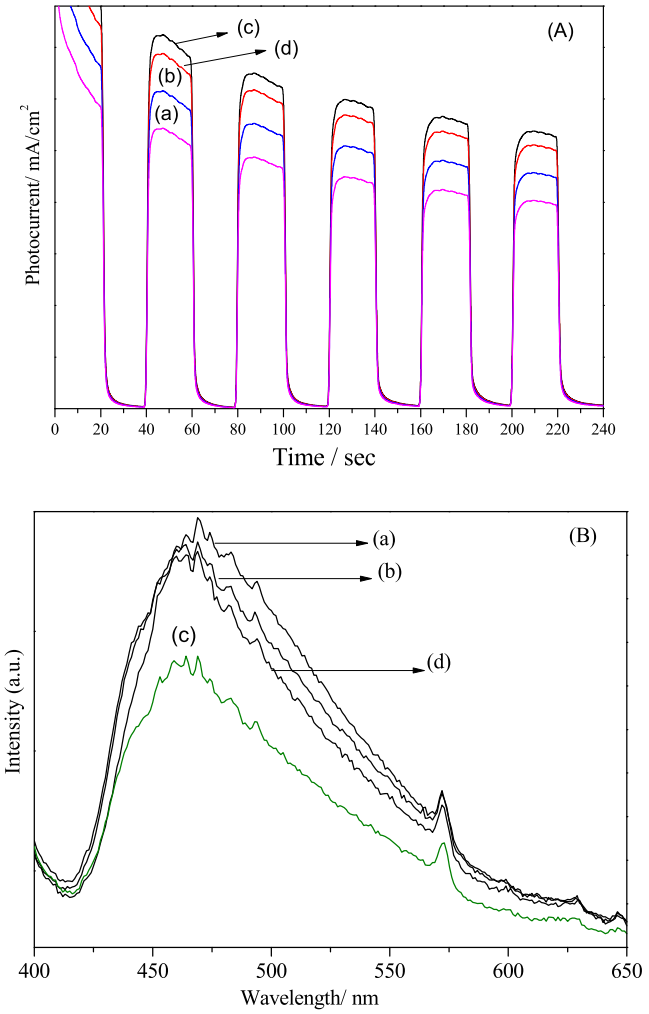

Figure 9. (A) Photocurrent density response of (a) $LaNaTaO_3$ and $LaNaTaO_3$ doped with RuO_2: (b) 1%, (c) 3%, and (d) 5%. (B) PL spectra of (a) $LaNaTaO_3$ and $LaNaTaO_3$ doped with RuO_2: (b) 1%, (c) 3%, and (d) 5%.

utilizing the assembly approach. To reduce possible changeability, the molar ratio of Ta^{5+}:F127:C_2H_5OH:HCl:CH_3COOH was maintained at 1:0.02:50:2.25:3.75. F-127 polymer surfactant (1.6 g) is added to 30 mL of C_2H_5OH using a magnetic stirrer at room temperature for 60 min; afterward, 0.74 mL of HCl and 2.3 mL of CH_3COOH were added to the clear solution F127 in ethanol, and then 1.82 g of $TaCl_5$ and 0.047 g of $La(NO_3)_3 \cdot xH_2O$ were added to the above mixture. Afterward, 3.5 g of CH_3COONa was added with stirring for 60 min to obtain $LaNaTaO_3$ perovskite. The mesophase was put in a Petri dish for drying at 110 °C for 24 h. The as-made mesophase was annealed at 450 °C for 4 h and then 650 °C for 4 h and annealed at 900 °C for 8 h in the air to obtain mesoporous $LaNaTaO_3$ perovskite. The synthesized $LaNaTaO_3$ perovskite (1 g) was suspended in 100 mL of ethanol, and a desired amount of ruthenium(III) acetylacetonate solutions containing the equivalent amount of Ru^{3+} was added to the suspension solution with sonication for 10 min to get 0.5, 1, 3, and 5% $RuO_2/LaNaTaO_3$ perovskites. The mixture was agitated magnetically for 3 h. The obtained samples were dried at 110 °C for 12 h and then annealed for 3 h at 450 °C to obtain mesoporous 0.5, 1, 3, and 5% $RuO_2/LaNaTaO_3$ perovskites.

Characterization of Mesoporous $RuO_2/LaNaTaO_3$ Perovskites. The detailed physicochemical characterization of the developed $RuO_2/LaNaTaO_3$ photocatalyst was performed to have a better understanding of composition, structure, and surface morphology of the perovskite photocatalysts. The X-ray diffraction pattern was measured through Cu $K\alpha_{1/2}$, $\lambda\alpha_1$ = 154.060 pm, $\lambda\alpha_2$ = 154.439 pm radiation using a Bruker AXS D4 Endeavour X diffractometer. Field emission secondary electron microscopy (FE-SEM) was conducted with an FE scanning electron microanalyzer (JEOL-6300F, 5 kV). The N_2 isotherm of the $RuO_2/LaNaTaO_3$ perovskites was performed at 77 K by analyzing adsorption isotherms with a Micromeritics ASAP 2010 volumetric adsorption unit. UV−vis diffuse reflectance spectra (DRS) of the $RuO_2/LaNaTaO_3$ perovskites were recorded on a UV−vis spectrophotometer (UV-2600, Shimadzu) at λ = 200−800 nm. A VG Escalab 200R electron spectrometer was applied to examine X-ray photoelectron spectra (XPS) for $RuO_2/LaNaTaO_3$ perovskites equipped with a Mg Kα X-ray source powered at 100 W. The C 1s peak at 284.8 eV was employed as calibration to estimate the binding energies (BE) of 1%$RuO_2/LaNaTaO_3$ perovskite.

H_2 Generation Experiments. Hydrogen generation was conducted in a continuous flow setup containing gas supply with a mass flow controller and a 100 cm^3 photoreactor quartz glass with a double jacket connecting a quadrupole mass spectrometer (QMS) for H_2 and O_2 detection. The QMS sampling rate is 1 cm^3 min^{-1}, facilitating a speedy H_2 and O_2 detection. Furthermore, this experimental setup provides an online recording of the whole course of the photocatalytic hydrogen generation with the utility of the simultaneous monitoring of the formation of H_2 and O_2 gases through the photocatalytic reaction. In the experimental series, 0.05 g of the synthesized $LaNaTaO_3$ photocatalyst was mixed in 50 mL of pure H_2O or 10 vol % CH_3OH aqueous solution and was sonicated to disperse the photocatalyst. Afterward, the photoreactor was locked and connected to the QMS through the stainless steel valves. An Ar gas flux was employed to eliminate the dissolved oxygen from the reactor with the 50 cm^3 min^{-1} flow rate for 10 min through the reactor to ensure there was O_2 or H_2 by the QMS. QMS was calibrated using standard H_2 and O_2 diluted in Ar. The flow rate of Ar gas at 10 cm^3 min^{-1} was fixed throughout the photocatalytic system at 25 °C. Before turning on illumination, the photocatalytic reactions with magnetic stirring were kept for 40 min for stabilizing the background of photocatalytic reactions and the baseline was recorded by QMS. Afterward, the suspension was illuminated for 3 h employing an Osram XBO 1000 W Xe arc lamp as a UV source, and it stood inside a Müller LAX parallel photoreactor. During illumination, the obtained H_2 or O_2 gases were monitored under steady-state conditions. After 3 h illumination, the 1000 W Xe arc was turned off permitting the photocatalytic system to get the baseline again.

AUTHOR INFORMATION

Corresponding Author

Adel A. Ismail − *Advanced Materials Department, Central Metallurgical R&D Institute, CMRDI, Helwan, Cairo 11421, Egypt;* orcid.org/0000-0002-5227-2644; Email: adelali141@yahoo.com

https://doi.org/10.1021/acsomega.1c00584
ACS Omega 2021, 6, 10250−10259

Authors

Maha Alhaddad − *Department of Chemistry, Faculty of Science, King Abdulaziz University, Jeddah 21589, Saudi Arabia*

Zaki I. Zaki − *Department of Chemistry, College of Science, Taif University, Taif 21944, Saudi Arabia*

Complete contact information is available at: https://pubs.acs.org/10.1021/acsomega.1c00584

Notes

The authors declare no competing financial interest.

■ ACKNOWLEDGMENTS

This work was financially supported by the Taif Researchers Supporting Project (TURSP-2020/42), Taif University, Taif, Saudi Arabia.

■ REFERENCES

(1) Akhundi, A.; Habibi-Yangjeh, A.; Abitorabi, M.; Pouran, S. R. Review on photocatalytic conversion of carbon dioxide to value-added compounds and renewable fuels by graphitic carbon nitride-based photocatalysts. *Catal. Rev.* **2019**, *61*, 595−628.

(2) Ismail, A. A.; Bahnemann, D. W. Photochemical splitting of water for hydrogen production by photocatalysis: A review. *Sol. Energy Mater. Sol. Cells* **2014**, *128*, 85−101.

(3) Kadi, M. W.; Mohamed, R. M.; Ismail, A. A.; Bahnemann, D. W. Decoration of mesoporous graphite-like C_3N_4 nanosheets by NiS nanoparticle-driven visible light for hydrogen evolution. *Appl, Nanosci.* **2018**, *8*, 1587−1596.

(4) Osterloh, F. E. Inorganic materials as catalysts for photochemical splitting of water. *Chem. Mater.* **2008**, *20*, 35−54.

(5) Castelli, I. E.; Landis, D. D.; Thygesen, K. S.; Dahl, S.; Chorkendorff, I.; Jaramillo, T. F.; Jacobsen, K. W. New cubic perovskites for one-and two-photon water splitting using the computational materials repository. *Energy Environ. Sci.* **2012**, *5*, 9034−9043.

(6) Vojvodic, A.; Nørskov, J. K. Optimizing perovskites for the water-splitting reaction. *Science* **2011**, *334*, 1355−1356.

(7) Zhang, G.; Liu, G.; Wang, L.; Irvine, J. T. Inorganic perovskite photocatalysts for solar energy utilization. *Chem. Soc. Rev.* **2016**, *45*, 5951−5984.

(8) Kato, H.; Kudo, A. Water splitting into H_2 and O_2 on alkali tantalate photocatalysts $ATaO_3$ (A= Li, Na, and K). *J. Phys. Chem. B* **2001**, *105*, 4285−4292.

(9) Kato, H.; Kudo, A. Photocatalytic water splitting into H_2 and O_2 over various tantalate photocatalysts. *Catal. Today* **2003**, *78*, 561−569.

(10) Liu, J. W.; Chen, G.; Li, Z. H.; Zhang, Z. G. Hydrothermal synthesis and photocatalytic properties of $ATaO_3$ and $ANbO_3$ (A= Na and K). *Int. J. Hydrogen Energy* **2007**, *32*, 2269−2272.

(11) Hu, C. C.; Tsai, C. C.; Teng, H. Structure characterization and tuning of perovskite-like $NaTaO_3$ for applications in photo-luminescence and photocatalysis. *J. Am. Ceram. Soc.* **2009**, *92*, 460−466.

(12) Li, X.; Zang, J. Facile hydrothermal synthesis of sodium tantalate ($NaTaO_3$) nanocubes and high photocatalytic properties. *J. Phys. Chem. C* **2009**, *113*, 19411−19418.

(13) Fu, X.; Wang, X.; Leung, D. Y.; Xue, W.; Ding, Z.; Huang, H.; Fu, X. Photocatalytic reforming of glucose over La doped alkali tantalate photocatalysts for H_2 production. *Catal. Commun.* **2010**, *12*, 184−187.

(14) Yokoi, T.; Sakuma, J.; Maeda, K.; Domen, K.; Tatsumi, T.; Kondo, J. N. Preparation of a colloidal array of $NaTaO_3$ nanoparticles via a confined space synthesis route and its photocatalytic application. *Phys. Chem. Chem. Phys.* **2011**, *13*, 2563−2570.

(15) Shi, J.; Liu, G.; Wang, N.; Li, C. Microwave-assisted hydrothermal synthesis of perovskite $NaTaO_3$ nanocrystals and their photocatalytic properties. *J. Mater. Chem.* **2012**, *22*, 18808−18813.

(16) Meyer, T.; Priebe, J. B.; da Silva, R. O.; Peppel, T.; Junge, H.; Beller, M.; Brückner, A.; Wohlrab, S. Advanced charge utilization from $NaTaO_3$ photocatalysts by multilayer reduced graphene oxide. *Chem. Mater.* **2014**, *26*, 4705−4711.

(17) Li, Y.; Gou, H.; Lu, J.; Wang, C. A two-step synthesis of $NaTaO_3$ microspheres for photocatalytic water splitting. *Int. J. Hydrogen Energy* **2014**, *39*, 13481−13485.

(18) Porob, D. G.; Maggard, P. A. Flux syntheses of La-doped $NaTaO_3$ and its photocatalytic activity. *J. Solid State Chem.* **2006**, *179*, 1727−1732.

(19) Yan, S. C.; Wang, Z. Q.; Li, Z. S.; Zou, Z. G. Photocatalytic activities for water splitting of La-doped-$NaTaO_3$ fabricated by microwave synthesis. *Solid State Ionics* **2009**, *180*, 1539−1542.

(20) Husin, H.; Chen, H. M.; Su, W. N.; Pan, C. J.; Chuang, W. T.; Sheu, H. S.; Hwang, B. J. Green fabrication of La-doped $NaTaO_3$ via H_2O_2 assisted sol−gel route for photocatalytic hydrogen production. *Appl. Catal., B* **2011**, *102*, 343−351.

(21) Li, X.; Zang, J. Hydrothermal synthesis and characterization of Lanthanum-doped $NaTaO_3$ with high photocatalytic activity. *Catal. Commun.* **2011**, *12*, 1380−1383.

(22) Iwase, A.; Kato, H.; Kudo, A. The effect of Au cocatalyst loaded on La-doped $NaTaO_3$ on photocatalytic water splitting and O_2 photoreduction. *Appl. Catal., B* **2013**, *136*−*137*, 89−93.

(23) Husin, H.; Su, W. N.; Chen, H. M.; Pan, C. J.; Chang, S. H.; Rick, J.; Chuang, W. T.; Sheu, H. S.; Hwang, B. J. Photocatalytic hydrogen production on nickel-loaded $La_xNa_{1-x}TaO_3$ prepared by hydrogen peroxide-water based process. *Green Chem.* **2011**, *13*, 1745−1754.

(24) Mohamed, R. M.; Ismail, A. A.; Basaleh, A. S.; ir, H. A. Photodeposition of Ag nanoparticles on mesoporous $LaNaTaO_3$ nanocomposites for promotion H_2 evolution. *Mater. Res. Bull.* **2020**, *131*, No. 110962.

(25) Mohamed, R. M.; Ismail, A. A. Mesoporous Pt/$La_{0.02}Na_{0.98}TaO_3$ nanocomposites as efficient photocatalyst for hydrogen evolution. *Mol. Catal.* **2020**, *486*, No. 110885.

(26) Mohamed, R. M.; Ismail, A. A.; Basaleh, A. S.; Bawazir, H. A. Construction of highly dispersed Nd_2O_3 nanoparticles onto mesoporous $LaNaTaO_3$ nanocomposites for H_2 evolution. *J. Photochem. Photobiol., A* **2020**, *400*, No. 112723.

(27) Mohamed, R. M.; Ismail, A. A.; Basaleh, A. S.; Bawazir, H. A. Facile fabrication of mesoporous In_2O_3/$LaNaTaO_3$ nanocomposites for photocatalytic H_2 evolution. *Int. J. Hydrogen Energy* **2020**, *45*, 19214−19225.

(28) Sudrajat, H.; Babel, S.; Thushari, I.; Laohhasurayotin, K. Stability of La dopants in $NaTaO_3$ photocatalysts. *J. Alloys Compd.* **2019**, *775*, 1277−1285.

(29) Iguchi, S.; Teramura, K.; Hosokawa, S.; Tanaka, T. A $ZnTa_2O_6$ photocatalyst synthesized via solid state reaction for conversion of CO_2 into CO in water. *Catal. Sci. Technol.* **2016**, *6*, 4978−4985.

(30) Qin, R.; Song, H.; Pan, G.; Bai, X.; Dong, B.; Xie, S.; Liu, L.; Dai, Q.; Qu, X.; Ren, X.; Zhao, H. Polyol-mediated synthesis of hexagonal LaF_3 nanoplates using $NaNO_3$ as a mineralizer. *Cryst. Growth Des.* **2009**, *9*, 1750−1756.

(31) Lee, Y.; Watanabe, T.; Takata, T.; Hara, M.; Yoshimura, M.; Domen, K. Hydrothermal synthesis of fine $NaTaO_3$ powder as a highly efficient photocatalyst for overall water splitting. *Bull. Chem. Soc. Jpn.* **2007**, *80*, 423−428.

(32) Nelson, J. A.; Wagner, M. J. Synthesis of sodium tantalate nanorods by alkalide reduction. *J. Am. Chem. Soc.* **2003**, *125*, 332−333.

(33) Lee, S.; Teshima, K.; Mizuno, Y.; Yubuta, K.; Shishido, T.; Endo, M.; Oishi, S. Growth of well-developed sodium tantalate crystals from a sodium chloride flux. *CrystEngComm* **2010**, *12*, 2871−2877.

(34) Yi, X.; Li, J. Synthesis and optical property of $NaTaO_3$ nanofibers prepared by electrospinning. *J. Sol-Gel Sci. Technol.* **2010**, *53*, 480−484.
(35) Lin, W. H.; Cheng, C.; Hu, C. C.; Teng, H. $NaTaO_3$ photocatalysts of different crystalline structures for water splitting into H_2 and O_2. *Appl. Phys. Lett.* **2006**, *89*, No. 211904.
(36) Liu, C.; Zou, B.; Rondinone, A. J.; Zhang, Z. J. Sol− gel synthesis of free-standing ferroelectric lead zirconate titanate nanoparticles. *J. Am. Chem. Soc.* **2001**, *123*, 4344−4345.
(37) Liu, J. W.; Chen, G.; Li, Z. H.; Zhang, Z. G. Hydrothermal synthesis and photocatalytic properties of $ATaO_3$ and $ANbO_3$ (A= Na and K). *Int. J. Hydrogen Energy* **2007**, *32*, 2269−2272.
(38) Fu, H.; Zhang, S.; Zhang, L.; Zhu, Y. Visible-light-driven $NaTaO_{3-x}N_x$ catalyst prepared by a hydrothermal process. *Mater. Res. Bull.* **2008**, *43*, 864−872.
(39) Shannon, R. D. Revised effective ionic radii and systematic studies of interatomic distances in halides and chalcogenides. *Acta Crystallogr., Sect. A* **1976**, *32*, 751−767.
(40) Ai, Z.; Ho, W.; Lee, S.; Zhang, L. Efficient photocatalytic removal of NO in indoor air with hierarchical bismuth oxybromide nanoplate microspheres under visible light. *Environ. Sci. Technol.* **2009**, *43*, 4143−4150.
(41) Gonçalves, R. V.; Wender, H.; Migowski, P.; Feil, A. F.; Eberhardt, D.; Boita, J.; Khan, S.; Machado, G.; Dupont, J.; Teixeira, S. R. Photochemical hydrogen production of Ta_2O_5 nanotubes decorated with NiO nanoparticles by modified sputtering deposition. *J. Phys. Chem. C* **2017**, *121*, 5855−5863.
(42) Sreethawong, T.; Ngamsinlapasathian, S.; Suzuki, Y.; Yoshikawa, S. Nanocrystalline mesoporous Ta_2O_5-based photocatalysts prepared by surfactant-assisted templating sol−gel process for photocatalytic H_2 evolution. *J. Mol. Catal. A: Chem.* **2005**, *235*, 1−11.
(43) Noda, Y.; Lee, B.; Domen, K.; Kondo, J. N. Synthesis of crystallized mesoporous tantalum oxide and its photocatalytic activity for overall water splitting under ultraviolet light irradiation. *Chem. Mater.* **2008**, *20*, 5361−5367.
(44) Ivanova, I.; Kandiel, T. A.; Cho, Y. J.; Choi, W.; Bahnemann, D. Mechanisms of photocatalytic molecular hydrogen and molecular oxygen evolution over La-doped $NaTaO_3$ particles: Effect of different cocatalysts and their specific activity. *ACS Catal.* **2018**, *8*, 2313−2325.
(45) Linsebigler, A. L.; Lu, G.; Yates, J. T., Jr. Photocatalysis on TiO_2 surfaces: principles, mechanisms, and selected results. *Chem. Rev.* **1995**, *95*, 735−758.
(46) Schneider, J.; Bahnemann, D. W. Undesired role of sacrificial reagents in photocatalysis. *J. Phys. Chem. Lett.* **2013**, *4*, 3479−3483.

https://doi.org/10.1021/acsomega.1c00584
ACS Omega 2021, 6, 10250−10259